On reversals in 2D turbulent Rayleigh-Bénard convection: Insights from embedding theory and comparison with proper orthogonal decomposition analysis

Davide Faranda, Berengere Podvin, Anne Sergent

To cite this version:

Davide Faranda, Berengere Podvin, Anne Sergent. On reversals in 2D turbulent Rayleigh-Bénard convection: Insights from embedding theory and comparison with proper orthogonal decomposition analysis. Chaos: An Interdisciplinary Journal of Nonlinear Science, 2019, 29, pp.033110. 10.1063/1.5081031 . hal-01701353v1

HAL Id: hal-01701353
https://hal.science/hal-01701353v1

Submitted on 5 Feb 2018 (v1), last revised 6 Feb 2019 (v2)

Reconciling embedding theorems and Proper Orthogonal Decomposition via the Rayleigh-Bénard convection

D. Faranda*
LSCE-IPSL, CEA Saclay l'Orme des Merisiers, CNRS UMR 8212 CEA-CNRS-UVSQ,
Université Paris-Saclay, 91191 Gif-sur-Yvette, France†

B. Podvin, A. Sergent
LIMSI-CNRS UPR 3251 BP133 Université Paris-Sud 91403 ORSAY CEDEX

We use Rayleigh-Bénard convection simulations to compare the properties of stationary states obtained via Principal Orthogonal Decomposition (POD) to those derived by embedding the global angular momentum of the system. We find that the results obtained with POD and embedding techniques provide the same information. The low computational costs of embedding analysis suggests to use this procedure whenever a global observable reflecting the symmetry of the system can be identified, while the POD should be preferred when such information is not available.

INTRODUCTION

In the last decades, the approach to the study of complex systems has shifted from a pure dynamical systems based approach to a mixture of statistical and statistical-mechanics techniques. This can be justified on both practical and theoretical levels. At the beginning of the 80s, the abundance of data from measurements as well as from numerical models was limited. The complex systems studied were mostly laboratory flows whose laminar or turbulent behavior depended on a control parameter[1, 2]. The use of numerical weather forecasts was limited to few days[3] and climate models were mostly conceptual[4]. At that time, new results in dynamical systems theory seemed to convince the scientific community that a sufficiently long time series could be sufficient to reconstruct the dynamics of the system via its attractor. This object is a geometric set toward which the system tends to evolve, even when starting from different initial conditions.

The Takens [5, 6] reconstruction theorem was then used to determine the dynamics of climate attractors as well as of complex flows. Initially the dimensions of these objects was set to be extremely low, usually smaller than 10 [7]. However, from the beginning of the 90s, several authors [8–10] found out that their optimistic estimates were wrong both because of the length of the time series used and of the nature of the observable used: in fact, despite the complexity of the systems, the reconstructions were mostly made using time series measured at specific points of the space. In parallel, computational power increased quickly [11] and measurement techniques opened new possibility to sample complex systems' behavior[12]. While in experiments visualization technology gave rapid access to fields measurements instead of local measurements[13, 14], numerical simulations were capable to produce long simulations of Earth's climate[15], human brain[16], molecules/proteins dynamics [17, 18].

The abundance of fields rather than single-point time series rapidly demanded for new statistical techniques capable to identify the metastable states of the systems and eventually forecasts the evolution of the systems. For this purpose, one of the most popular statistical technique used was (and is still nowadays) the Proper Orthogonal Decomposition (POD). The idea is to use an orthogonal transformation to transform a dataset with correlated variables into linearly uncorrelated variables. Geometrically, this is like f fitting an n-dimensional ellipsoid to the data, where each axis of the ellipsoid represents a principal component.

Principal Component Analysis was invented by Karl Pearson[19], as an analogue of the principal axis theorem in mechanics. In the 1930s it was developed independently also by Harold Hotelling [20]. Depending on the field of application, it is also named the discrete Kosambi-Karhunen-Loève transform (KLT) in signal processing [21], the Hotelling transform [20] in multivariate quality control, proper orthogonal decomposition (POD) in turbulence [22], empirical orthogonal functions (EOF) in meteorological science [23], empirical eigenfunction decomposition [24], and it is also connected to singular value decomposition (SVD) of X [25], eigenvalue decomposition (EVD) of XTX in linear algebra, factor analysis, Eckart-Young theorem [26], or Schmidt-Mirsky theorem in psychometrics, quasiharmonic modes [27], spectral decomposition in noise and vibration, and empirical modal analysis in structural dynamics [28].

The popularity and usefulness of this technique, the fact that embedding theorems could not be applied either to systems featuring a large number of degrees of freedom either on fields time series, caused the data analysis scientific community to prefer the statistical approach based on the POD. On the other hand, there were several theoretical developments in dynamical systems theory directed towards understanding how to deal with systems with large numbers of degrees of freedom[29, 30]. In particular, the framework of stochastic dynamical systems [31, 32] bring into the field the idea that the dynamics of complex systems can be represented by a small number of variables if one lumps the noise contributions into noise terms and choice as observables for the embedding procedure, global quantities tracking symmetry properties of the flow.

On turbulent flow, as the von Karman swirling flow, or in atmospheric dynamics, this revised approach produces phase portraits which allow for the definition of low dimensional models capturing the essential featuring of the dynamics[33] in the fashion of the Lorenz 1963 equations [34]. It is then time to reconcile the POD approach with the embedding theorems, define a correspondence between the dynamics identified with the two methods and assess how one approach can complete rather than substitute the other. To this purpose we will use extensive numerical simulations of the Rayleigh Bénard convection, a problem that motivates Lorenz to define its butterfly[34].

The paper is structured as follow: first we will recap the methodologies used, with emphasis on the recent developments on the embedding strategies for complex systems. Then we will describe the dataset used and outline the results. Eventually we will discuss the advantage of a combined approach to complex systems analysis.

DYNAMICAL SYSTEMS METHODS

In this section we give some elements of dynamical systems theory and some guidelines derived from recent studies for reconstructing the attractors using global rather than local observables. We also introduce indicators of stability derived from the theory of stochastic processes.

Observable choice for embedding

It has beeen proved that it is possible to describe the large scale motion of a fully-developed turbulent flow with few degrees of freedom, if an appropriate observable reflecting the flow symmetry is selected. The large embedding dimensions which prevented the applications of dynamical systems theory to turbulence arise from small scale disturbances can be modeled in terms of stochastic perturbations. This general picture reconciles the Landau [35] and Ruelle-Takens [36] descriptions of turbulence, the former being valid at small scales, and the latter describing the large scale motions. The observable can be derived as global mean of some local quantities in the flow (average energy or momentum), or it can be a single global quantity measured in an experiment (in the von Karman swirling flow, the torque applied to the motors has been used for reconstructing the attractor).

Attractor Reconstruction

There are different embedding procedures used to reconstruct phase portrait from a signal. The first thing to determine is the embedding dimension, i.e. the number of variables necessary for the attractor reconstruction. This can be done using the method by Cao, or by trying to see how much information is added using another dimension. This kind of information can be also extracted by a POD analysis. The series of the global observable is then embedded with the methods of the delays [5], or the local peaks procedure [37]. The local peaks method allow to select only the robust feature of the attractor discarding the noisy part, which will make the attractor looks fuzzy. We prefer the local peaks embedding procedure , by extraction of the maxima M_m (or minima since the results do not change significantly) under the condition that subsequent maxima cannot fall within 10 Hz (see Fig. 4 in [32] for the portraits reconstructed with the delay methods [5]). Once the series of partial maxima is obtained, the attractor is visualized by plotting in a n-dimensional phase space, M_m, M_{m+1}, ..., M_{m+n}. The value of n, known as the embedding dimension, plays a crucial role in the applications of dynamical systems theory to real data [38].

Stability indicator

To characterize the stability of the attractor, we will use the indicator Υ introduced in [39]. We define our stability indicator by using a simple example: even for a complex system, the dynamics near a metastable state resembles to that of a stochastic spring (or of a particle in a quadratic potential). The typical equation associated to those system is the Langevin equation:

$$\frac{\mathrm{d}X(t)}{\mathrm{d}t} = -\frac{k}{m}X(t) + \frac{1}{m}\xi(t)$$

with k a frictional force (e.g. the Stokes' drag), m the mass of the particle and ξ a noise term modeling random collisions the particle undergoes. The discretized equation then becomes:

$$X_t = \phi X_{t-1} + \epsilon_t$$

which is an ARMA(1,0). ARMA stands for Autoregressive Moving-average model, a class of linear processes. It has been widely used over the past decades, especially in econometrics and finance to forecast markets trends. We briefly show the normal form of an ARMA(p,q) model and some criteria used to fit it to a time series (see [40] for a detailed review).

Let us consider a series $X(t)$ of an observable with unknown underlying dynamics. We further assume that for a time scale τ of interest, the time series X_{t_1}, X_{t_2}, ..., $X_{t\tau}$ represents a stationary phenomenon. Since X_t is stationary, we may then model it by an ARMA(p, q) process such that for all t:

$$X_t = \sum_{i=1}^{p} \phi_i X_{t-i} + \varepsilon_t + \sum_{j=1}^{q} \theta_j \varepsilon_{t-j}$$

with $\varepsilon_t \sim WN(0, \sigma^2)$ - where WN stands for white noise - and the polynomials $\phi(z) = 1 - \phi_1 z_{t-1} - ... - \phi_p z_{t-p}$ $\theta(z) = 1 - \theta_1 z_{t-1} - ... - \theta_q z_{t-q}$, with $z \in \mathbb{C}$, have no common factors. Notice that, hereinafter, the noise term ε_t is assumed to be a white noise. For a general stationary time series, this model is not unique. However there are several standard procedures for selecting the model which fits at best the data. The one we exploit is the Bayesian information criteria [41]. It is based on the Akaike information criteria (AIC) [42] which was designed to be an approximately unbiased estimate of the Kullback–Leibler index of the fitted model relative to the true model. Assuming we know the likelihood estimators β and σ^2 of the fitted model model thanks to an innovation algorithm, our ARMA model is the one where p and q minimize

$$\mathrm{AIC}(\beta) = -2 \ln L_X(\beta, \sigma^2) + 2(p + q + 1)$$

In order to correct the tendency of the AIC to prefer complex models, we use the BIC (Bayesian information criteria) which introduces a penalty for large-order models:

$$\mathrm{BIC} = (\tau - p - q) \ln \left(\frac{\tau \sigma^2}{\tau - p - q} \right) + \tau (1 + \ln \sqrt{2\pi}) + (p + q) \ln \left(\left(\sum_{t=1}^{\tau} X_t^2 - \tau \sigma^2 \right) / (p + q) \right)$$

Intuitively, p and q are related to memory lag of the process, while the coefficients ϕ_i and θ_i represent the persistence: the higher their sum (in absolute value), the slower the system is in forgetting its past history, the higher the correlations in the time series. Most of the time ARMA models are used in econometrics fitting the whole time series and trying to forecast the future trend of the variable. This assumes a correlation with the past and provide some significant results for the very near future. Our interest is rather to use ARMA to detect the local stability. The procedure is the same as for fitting the whole time series: after slicing the time series by intervals τ, we obtain a time series $X_{t-\tau}$, ..., X_{t-1}. We then fit each ARMA(p,q) model until $p \leq p_{max}$ and $q \leq q_{max}$ assessing the best one (according the BIC criterion). We then compute the stability indicator Υ for the system at time t and then move to time $t + 1$ to perform the same analysis on the time series $X_{t-\tau+1}$, ..., X_t.

When the system is close to an unstable point, separating multiple basins of attraction, the behavior cannot be described by a Langevin equation as the underlying potential is not quadratic anymore. The change in the shape of the potential introduces new correlation in the time series resulting in higher order ARMA terms. The indicator is then defined as:

$$\Upsilon = 1 - \exp \frac{|\mathrm{BIC}(p, q) - \mathrm{BIC}(1, 0)|}{\tau}$$

Thus, Υ gives us a normalized distance between the stablest state the particle could be in ($\Upsilon = 0$) and the state where it really is. The limit $\Upsilon \longrightarrow 1$ correspond to a very unstable state, where the particle is a the edge of a basin

of attraction and the probability to jump to another connected basin is high.
The only free parameter is the choice of τ. To understand its role, we revert to the spring example: the characteristic time scale of the problem is the relaxation time of the particle to the basin of attraction. This define the typical time scale of the system. The Δt between subsequent observation of the time series should be close to this quantity. Instead, τ must be a multiple of this quantity but should be smaller than the residence time in the basin of attraction. In previous works, some of the authors of this paper have shown the validity of the Υ indicator to study financial [39] and climate time series [43].

POD ANALYSIS

Proper Orthogonal Decomposition is a statistical technique that extracts the most energetic spatial flow patterns. Any physical field can thus be written as the superposition of an infinite number of spatial modes, the amplitude of which varies in time. The full state of the flow at a given time can then be represented by the instantaneous amplitudes of the spatial eigenfunctions. Any physical quantity $\underline{q}(\underline{x}, t)$ can be decomposed into the superposition of an infinity of spatial structures $\underline{\phi}$, the amplitude of which varies in time:

$$\underline{q}(\underline{x}, t) = \sum_{n=1}^{\infty} a^n(t)\underline{\phi}^n(\underline{x}) \tag{1}$$

where the $\underline{\phi}^n(x)$ are eigensolutions of the eigenvalue problem

$$\int R(\underline{x}, \underline{x}').\underline{\phi}(\underline{x}')d\underline{x}' = \lambda^n \underline{\phi}(\underline{x}) \tag{2}$$

where $R(\underline{x}, xx')$ is the spatial autocorrelation tensor at zero time lag. The associated eigenvalues $\lambda^n =< (^n)^2 >$, where $<>$ represents a temporal average, correspond to the energy level of the n-th spatial eigenfunction. By construction, the amplitudes a^n are uncorrelated and the spatial eigenfucntions orthogonal. POD therefore naturally provides a dynamical systems representation $\{a^n(t)\}$ of the flow. The representation is energetically optimal, to the extent that any POD truncation of a given dimension captures at least as much energy as any other decomposition.

The spatial eigenfunctions are extracted from the second-order statistics of $\underline{q}$, so that Proper Orthogonal Decomposition requires an extensive knowledge of the fully resolved flow and acts as a powerful data reduction technique. It is therefore of interest to compare results from this approach with the embedding technique, which is based on limited data and aims to reconstruct dynamical information from a single time-series.

RAYLEIGH-BÉNARD CONVECTION

We compare POD and dynamical systems based techniques on a turbulent Rayleigh-Bénard convective flow in a square (2-D) cell (see figure 1). This flow represents a canonical configuration which displays random large-scale pattern changes in the presence of small-scale fluctuations. The top and the bottom plate of the cell are maintained at different temperatures, with a hotter bottom plate and colder top one. This leads to the generation of temperature plumes along the plates, which detach from the boundary layer and are transported into the flow. The natural convection flow in the square cell is characterized by two parameters. One is the Prandtl number $Pr = \nu/\kappa$ where ν is the kinematic viscosity and κ the thermal diffusivity. Here we consider water ($Pr = 4.3$). The other is the Rayleigh number $Ra = \frac{\alpha g \Delta T H^3}{\nu\kappa}$ which measures the ratio of buoyancy and diffusive effects, with α the thermal expansion coefficient, g the gravity, ΔT the temperature difference between the plates, H the dimension of the cell. Adiabatic boundary conditions are imposed on the cell sides.

The flow is numerically simulated in the Boussinesq approximation using a spectral code. The simulation parameters are given in table I. The equations are made nondimensional using as characteristic units the cell height H for length, the temperature difference ΔT for temperature and the convective velocity $Ra^{1/2}\kappa/H$ for velocity. More details on the numerical simulation can be found in [44]. Three different Rayleigh numbers $Ra = 3\ 10^7$, $Ra = 5\ 10^7$ and $Ra = 10^8$ are considered in the present study. Figure 1 shows two typical flow realizations at $Ra = 5\ 10^7$. One can see that the small-scale plumes collect together and form a large-scale circulation. However the large-scale circulation can take two different orientations. The flow will take one orientation during a long period of time (for instance figure 1 a), then will switch rapidly and apparently randomly towards the state of opposite orientation (figure 1 b)). The occurrence and frequency of reversals depends on the Rayleigh number and the Prandtl number as shown by Sugiyama *et al* [45]. Reversal processes in 2-D or near 2-D cells have been the object of several investigations (Sugiyama *et al.* [45], Chandra *et al.*, [46], Ni *et al.* [47]), while several models have also been derived for reversals occuring in a cylinder cell (Brown and Ahlers [48], Sreenivasan et al. Araujo *et al.* [49, 50], Benzi [51]). More recently, Podvin and Sergent [44], [52] have used Proper Orthogonal Decomposition (POD) to construct dynamical systems to reproduce reversals in the square 2-D cell. By use of a time rescaling of the temporal series, Castillo *et al.* [53] have evidenced a generic reversal cycle consisted of three successive phases.

RESULTS

POD spectrum

In previous works [44], [52], we have used POD to investigate the large-scale structure of the flow. Proper Orthogonal Decomposition was applied to the joint temperature and velocity fields at three different Rayleigh numbers. The number of snapshots and separation between snapshots used in the sudy is given in table I. We checked that at all Rayleigh numbers the first four modes corresponded to the same spatial structures, described in [52]. The amplitude of the dominant mode a^1, which corresponds to a one-cell large-scale circulation all around the square, is shown in Figure 2 It is well correlated with the global angular momentum L (with a correlation coefficient larger than 0.95). This confirms that the choice of the global angular momentum L is relevant to carry out the analysis. The first four modes of the POD capture more than 85% of the total energy. The full eigenvalue spectrum is represented in Figure 3 and shows that the energy in the first modes is similar for $Ra = 5\ 10^7$ and $Ra = 10^8$ and larger than at $Ra = 3\ 10^7$. However table II shows that the different behaviors for different Rayleigh numbers do not correspond to a global increase in the energy of small scales. This suggests that the increase of the reversal frequency is associated with a higher energy in the low-order modes, and in particular mode 3, which table III is 8 times more energetic at the two highest Rayleigh numbers, while the energy of all other modes is only twice as large, but does not seem to be associated with a larger energy content in the small scales.

Phase portraits

POD Phase portraits of the system for normalized coefficients are given in Figures 4 to 6. The system spends a large portion of the time near one of the quasi-stable states (corresponding to a set large-scale circulation), then makes excursions from one of the quasi-stable states to the other. Again, despite similarities, differences between the Rayleigh numbers are clear. As the Rayleigh number increases, the second mode takes negative values during excursions (Figure 4). The amplitude of the third mode is larger during excursions (Figure 5) for the lowest Rayleigh number. At $Ra = 5\ 10^7$ (and to some extent for $Ra = 3\ 10^7$), the system appears to spend a good portion of the time near $a^1 = 0$, which corresponds to a state where the large-scale circulation has disappeared. This is less present at $Ra = 10^8$, where the presence of a limit cycle appears most probable, as can be seen in particular by comparing the different phase portraits in the (a^1, a^4) space. The phase portraits can be compared with the embedding portraits represented for three different Δt in Figure 9. The dynamics consists of two main fixed points, symmetric and located at $|L| \simeq 0.06$, and two marginal fixed points at $|L| \simeq 0.02$. They are connected by two limit cycles. By increasing the Rayleigh number (bottom panels) it is evident that the stability of the fixed points decreases and the dynamics consist of limit cycles rather than fixed points. One can see that both limit cycles and fixed points are identified with the POD representation (Figures 4 to 6). While at $Ra = 3 \cdot 10^7$, the two main fixed points are identifiable, their structure becomes more stretched and circular as Ra increases. It is interesting to relate these findings to the predictions reported in [44] and [52] for two models derived from the POD at $Ra = 5\ 10^7$ with respective dimensions of 3 and 5. The dynamics of the three-dimensional model was characterized by heteroclinic connections ([44]), which formed a cycle in the presence of noise, while the five-dimensional model (with two extra modes) displayed a limit cycle ([52]).

In the embedding method, we find that the optimal embedding dimension for the attractor is 2, which implies that two changes from one state to another are independent. This is an important result, which is in agreement with the idea that reversals occur independently from each other and that the time between reversals can be modeled with a Poisson distribution, which was experimentally observed for reversals in cylinder cells by Xi and Xia [54] and Brown et al. [48]. This is in contrast with the results found for the Von Karman flow [33]. For this flow, the attractor is 3D which suggests that subsequent reversals are not independent.

Stability analysis

We compute the stability parameter Υ using the following procedure: i) we coarse grain the time series of L at the three different $\Delta t = 3, 6, 9$ used for the attractor reconstruction, ii) for each of the value $L(t)$ obtained, we used the time series $L(t-\tau), L(t+1-\tau), ...L(t)$ where $t \geq \tau$ to compute Υ. Note that we fix $\tau = 50$ for the statistical needs outlined in [39].

The values of Υ for each point of the time series and different Δt are reported in Figures 10-12. The histogram of Υ and the bivariate histogram L, Υ are reported in figure 13. Overall, we remark that there is a general agreement among the results obtained at different Δt. For $Ra = 3\ 10^7$, most of the values of Υ are close to 0, as the dynamics is that of a noisy fixed points. During the reversal and immediately after the values of Υ are higher, indicating the switching of the dynamics. This is why Υ histograms (Figure 13 left) show a principal mode for low value of Υ and a small mode at higher values. The dynamics is different for the cases $Ra = 5\ 10^7$ and $Ra = 1\ 10^8$ as for the presence of the limit cycle. The periodicity of the reversals and the sporadic presence of a noisy fixed points dynamics leads to a general increase of Υ values.

Time between reversals

A characteristic of the flow reversals can be given by the time separating zeros of the amplitude of the dominant mode. The distribution of these times, normalized by their time-averaged value, which can be found in table II, is shown in Figure 7. The mean values of the separation times are very similar at the two highest Rayleigh numbers, while the mean value is higher by a factor of 10 in the case $Ra = 3\ 10^7$. However, the shape of the time distribution changes with each Rayleigh number. The low values of the separation times observed at all Rayleigh numbers correspond to times which are smaller than a full transition time (i.e a complete switch from one metastable state to another). This means that there is no real reversal corresponding to these separation times: either the flow switches back to its former state, or it remains around zero for a while, which corresponds to the temporary disappearance of a large-scale circulation. In agreement with the POD and the embedding phase portraits, these low values are frequent at $Ra = 3\ 10^7$ and $Ra = 5\ 10^7$, but less so at $Ra = 10^8$. One can see that the distributions at $Ra = 5\ 10^7$ and $Ra = 10^8$ present two local maxima. One is associated with the relatively low value mentioned above. The other is associated with a higher value, and corresponds to a long-lived switch from one metastable state to the other. A restriction of the histograms of the normalized time separation to the period $[0, 1]$ is represented in Figure 8 for the different Rayleigh numbers. It is of interest to compare these histograms, which are obtained from the full time-series and over long periods of time, with the distributions of the indicator Υ shown in Figure 13, which is extracted from application of the autoregressive model over a short period of time. Strong similarities are present, which supports the idea that the Υ indicator is able to discriminate between the true reversals of the flow (higher values) from shorter-lived transitions (lower values).

Attractors and representative flow patterns

We retain the local peaks method for reconstructing attractors. But taking advantage of previous knowledge about the physical response of the system [44, 53], we tune the peak identification process accordingly with physical considerations. First we extract the partial maxima from the time series of the absolute value of the angular momentum $|L|$. In order to avoid pointing a local peak during the transition period τ_d between two plateaus, we add a specific criteria: two successive maxima must be at least separated by twice the transition duration (see [44] for definition), which differs with the Rayleigh number. The corresponding attractors are shown in Figure 14.

As expected, most of the points corresponding to the (M_{i-1}, M_i) pairs are located close to the main diagonal for large $|L|$ values. This is particularly obvious at $Ra = 3 \cdot 10^7$ where the L plateaus (i.e. fixed points) are very extended in time. Additional points show the path (limit cycle) between the opposite plateaus and point out transitional states in the quadrants of opposite signs. Fewer points are plotted in the centre of the figure. They seems approximately equally distributed on the four quadrants for smaller $|L|$ values. For the two highest Rayleigh numbers attractors display more complex patterns. Transition path is still present. But points appears clustering around specific locations along the transition path as well as at the diagram centre.

Figure 15 shows a rough attempt of clustering the (M_{i-1}, M_i) pairs for $Ra = 5 \cdot 10^7$, as well as the representative flow patterns of the M_{i-1} and M_i states, estimated from a conditional averaging over each cluster. Twice five clusters have been identified which obey to a centrosymmetry in the (M_{i-1}, M_i) diagram: two fixed points at $|L| \simeq |\bar{L}| + \sigma(|L|)$ ($|\bar{L}|$ and $\sigma(|L|)$ being the mean $|L|$ value and its standard deviation over the whole time series), two marginal fixed points at $|L| \lesssim |\bar{L}| - \sigma(|L|)$, and six clusters describing particular steps during the cycle limit. As previously mentioned, the most dense clusters (in blue on the figure 15) which are located close to the main diagonal, are closely related to the two main fixed points i.e. plateaus. The evolution of the flow pattern between M_{i-1} and M_i states exhibits the growth of the corner flows. This physical phenomenon has been already identified in the literature (for example see [44, 45]) and associated to the accumulation phase of the generic reversal cycle in [53]. This is clearly shown on figure 16, where examples of (M_{i-1}, M_i) pairs are marked for each cluster on a particular sequence of the angular momentum time series at $Ra = 5 \cdot 10^7$. The orange cluster highlights the first part of the transition period (called the release phase in [53]), as the M_i states point out the rebound instant of the transition on figure 16. On the contrary red clusters encompass the whole release phase from the reversal phenomenon to the following step consisting of the flow pattern reorganisation into the main diagonal roll surrounding by two smaller corner flows. The next cluster (in green) corresponds to the acceleration phase of the reversal cycle, where the large diagonal roll is being strengthened. Finally central clusters (in magenta) reveal the relative importance of the cessation regime in comparison to the plateau regime in L time series. This regime is characterized by the disappearance of the main diagonal roll[44]. Figure 16 shows that the magenta points match well with rapid oscillations of $|L|$ peaks close to zero which is typical of cessations.

The clustering process has been applied similarly to both other attractors (figures 17, 18). It is noteworthy that the cluster shapes are quite similar whatever the Rayleigh number, as well as the corresponding representative flow patterns. However it can be noted that most clusters at $Ra = 3 \cdot 10^7$ does not contain a sufficient number of points to obtain a clear convergence of the representative flow patterns. Nonetheless the relative density of the clusters illustrates the relative time duration of different phases (as seen in figure 19). It shows shorter plateaus regarding the transition duration τ_d (stability decrease of the two main fixed points) as Ra increases, or the infrequency of cessations at $Ra = 3 \cdot 10^7$ and 10^8 . At all Ra, the M_{i-1} representative flow patterns of the clusters related to the release phase (in orange or red) point out a specific flow pattern where the corner flows occupy at least half the cavity width along the top or bottom wall. This feature is typical of the precursor event as noted in [52, 53]. Consequently this methodology of snapshots classification appears to be able to discriminate the different regimes of reversal or cessation [44] and the successive phases of standard reversals[52, 53] as previously identified by using different techniques.

DISCUSSION

In this work we have compared the results obtained with POD and embedding techniques on simulations of the Rayleigh-Bénard convection in a 2D cell at three different Rayleigh numbers. Our analysis suggests that significant information on the structure of the stationary states and their stability can be recovered by the embedding technique, which can be applied on-line to the time series of a single observable. The results are consistent with POD analysis (phase space characterization of reversals) and also with experimental observations (independence of reversals). Moreover, the position on the attractor can be used as a precursor of the subsequent phases of the dynamics. On the one hand, the embedding/dynamical systems approach is clearly of interest when the time series corresponds to a global observable tracing the symmetry of the system, such as the angular momentum in the Rayleigh Benard convection in the present case or the reduced frequency of rotation in the von Karman Flow [33]. Once the observable is identified it is a matter of seconds to embed the data and only a few minutes of CPU time on a laptop is needed to compute the stability Υ. On the other hand, in some systems such as the atmospheric or oceanic circulation, it can be difficult to identify directly a single symmetry parameter and, in this case POD analysis can be helpful to identify the relevant variables to which the embedding technique could be applied. When possible, a robust description of the system can be obtained by combining the two techniques.

ACKNOWLEDGEMENTS

This work was performed using HPC resources from GENCI-IDRIS (Grant 2a0326). DF was supported by ERC grant No. 338965.

---

[*] Electronic address: davide.faranda@cea.fr
[†] London Mathematical Laboratory, 14 Buckingham Street, London WC2N 6DF, UK

[1] J.-P. Eckmann, Reviews of Modern Physics **53**, 643 (1981).
[2] P. Bergé, Y. Pomeau, and C. Vidal, *Order within chaos* (Wiley and Sons NY, 1984).
[3] I. Mason, Aust. Meteor. Mag **30**, 291 (1982).
[4] R. Benzi, G. Parisi, A. Sutera, and A. Vulpiani, Tellus **34**, 10 (1982).
[5] F. Takens, in *Dynamical systems and turbulence, Warwick 1980* (Springer, 1981), pp. 366–381.
[6] L. Noakes, International Journal of Bifurcation and Chaos **1**, 867 (1991).
[7] K. Fraedrich, Journal of the atmospheric sciences **43**, 419 (1986).
[8] E. N. Lorenz, Nature **353**, 241 (1991).
[9] A. Tsonis, J. Elsner, and K. Georgakakos, Journal of the atmospheric sciences **50**, 2549 (1993).
[10] P. Holmes, J. L. Lumley, and G. Berkooz, *Turbulence, coherent structures, dynamical systems and symmetry* (Cambridge university press, 1998).
[11] F. Molteni, R. Buizza, T. N. Palmer, and T. Petroliagis, Quarterly journal of the royal meteorological society **122**, 73 (1996).
[12] F. Daviaud, J. Hegseth, and P. Bergé, Physical review letters **69**, 2511 (1992).
[13] K. Hinsch, OPTICAL ENGINEERING-NEW YORK-MARCEL DEKKER INCORPORATED- **38**, 235 (1993).
[14] J. G. Santiago, S. T. Wereley, C. D. Meinhart, D. Beebe, and R. J. Adrian, Experiments in fluids **25**, 316 (1998).
[15] M. Cullen, Meteorological Magazine **122**, 81 (1993).
[16] M. Hämäläinen, R. Hari, R. J. Ilmoniemi, J. Knuutila, and O. V. Lounasmaa, Reviews of modern Physics **65**, 413 (1993).
[17] J. Haile, *Molecular dynamics simulation*, vol. 18 (Wiley, New York, 1992).
[18] P. J. Steinbach and B. R. Brooks, Proceedings of the National Academy of Sciences **90**, 9135 (1993).
[19] K. Pearson, The London, Edinburgh and Dublin Philosophical Magazine and Journal **6**, 566 (1901).
[20] H. Hotelling, Journal of educational psychology **24**, 417 (1933).
[21] D. Kosambi, in *DD Kosambi* (Springer, 2016), pp. 115–123.
[22] B. Podvin and J. Lumley, Journal of Fluid Mechanics **362**, 121 (1998).
[23] E. N. Lorenz (1956).
[24] L. Sirovich, Quarterly of applied mathematics **45**, 561 (1987).
[25] G. H. Golub and C. F. Van Loan, Press, Baltimore (1983).
[26] H. H. Harman (1960).
[27] B. R. Brooks, D. Janežič, and M. Karplus, Journal of computational chemistry **16**, 1522 (1995).
[28] N. E. Huang, Z. Shen, S. R. Long, M. C. Wu, H. H. Shih, Q. Zheng, N.-C. Yen, C. C. Tung, and H. H. Liu, in *Proceedings of the Royal Society of London A: Mathematical, Physical and Engineering Sciences* (The Royal Society, 1998), vol. 454, pp. 903–995.
[29] R. Bagley and L. Glass, Journal of Theoretical Biology **183**, 269 (1996).
[30] R. Temam, *Infinite-dimensional dynamical systems in mechanics and physics*, vol. 68 (Springer Science & Business Media, 2012).
[31] L. Arnold, *Random dynamical systems* (Springer Science & Business Media, 2013).
[32] M. D. Chekroun, H. Liu, and S. Wang, *Approximation of Stochastic Invariant Manifolds: Stochastic Manifolds for Nonlinear SPDEs I.* (Springer, 2015).
[33] D. Faranda, Y. Sato, B. Saint-Michel, C. Wiertel, V. Padilla, B. Dubrulle, and F. Daviaud, arXiv preprint arXiv:1607.08409 (2016).
[34] E. N. Lorenz, Journal of the atmospheric sciences **20**, 130 (1963).
[35] L. D. Landau, in *Dokl. Akad. Nauk SSSR* (1944), vol. 44, pp. 339–349.
[36] D. Ruelle and F. Takens, Communications in mathematical physics **20**, 167 (1971).
[37] N. H. Packard, J. P. Crutchfield, J. D. Farmer, and R. S. Shaw, Physical review letters **45**, 712 (1980).
[38] H. Kantz and T. Schreiber, *Nonlinear time series analysis*, vol. 7 (Cambridge university press, 2004).
[39] D. Faranda, F. M. E. Pons, E. Giachino, S. Vaienti, and B. Dubrulle, Communications in Nonlinear Science and Numerical Simulation **29**, 233 (2015).
[40] S.-H. Poon and C. W. Granger, Journal of economic literature **41**, 478 (2003).
[41] H. Akaike, Applied Time Series Analysis pp. 1–23 (1978).
[42] H. Akaike, in *Selected Papers of Hirotugu Akaike* (Springer, 1998), pp. 199–213.
[43] D. Faranda and D. Defrance, Earth System Dynamics **7**, 517 (2016), URL `http://www.earth-syst-dynam.net/7/517/2016/`.
[44] B. Podvin and A. Sergent, Journal of Fluid Mechanics **766**, 172 (2015).

[45] K. Sugiyama, R. Ni, R. J. Stevens, T. S. Chan, S.-Q. Zhou, H.-D. Xi, C. Sun, S. Grossmann, K.-Q. Xia, and D. Lohse, Physical review letters **105**, 034503 (2010).
[46] M. Chandra and M. K. Verma, Physical review letters **110**, 114503 (2013).
[47] R. Ni, S.-D. Huang, and K.-Q. Xia, Journal of Fluid Mechanics **778**, R5 (2015).
[48] E. Brown, A. Nikolaenko, and G. Ahlers, Physical review letters **95**, 084503 (2005).
[49] K. R. Sreenivasan, A. Bershadskii, and J. Niemela, Physical Review E **65**, 056306 (2002).
[50] F. F. Araujo, S. Grossmann, and D. Lohse, Physical review letters **95**, 084502 (2005).
[51] R. Benzi, Physical review letters **95**, 024502 (2005).
[52] B. Podvin and A. Sergent, Physical Review E **95**, 013112 (2017).
[53] A. Castillo-Castellanos, A. Sergent, and M. Rossi, Journal of Fluid Mechanics **808**, 614 (2016).
[54] H.-D. Xi and K.-Q. Xia, Physics of Fluids **20**, 055104 (2008).

Ra	(N_x, N_z)	Δt	$N_{snapshots}$	$\Delta T_{snapshots}$	N_{total}
$3\ 10^7$	(159,385)	$6\ 10^{-4}$	825	6	12000
$5\ 10^7$	(159,385)	$6\ 10^{-4}$	825	6	12000
10^8	(201,513)	$3\ 10^{-4}$	660	4.5	8000

TABLE I: Simulation and POD analysis characteristics ar different Rayleigh numbers : numerical resolution, time step, number of snapshots used to extract the POD eigenfunctions, time separation between snapshots, total number of snapshots considered in the time series

Ra	$\sum_{\lambda \geq 5} / \sum_{\lambda}$	$< T >$
$3\ 10^7$	0.09	1160
$5\ 10^7$	0.12	203
10^8	0.10	195

TABLE II: POD Characteristics at different Rayleigh numbers. $< T >$ is defined as the time-averaged value separating two zeros of a^1 and is expressed in convective time units.

Ra	λ^1	λ^2	λ^3	λ^4
$3\ 10^7$	0.7	0.13	0.02	0.01
$5\ 10^7$	1.15	0.26	0.17	0.05
10^8	1.07	0.26	0.15	0.05

TABLE III: POD first eigenvalues at different Rayleigh numbers.

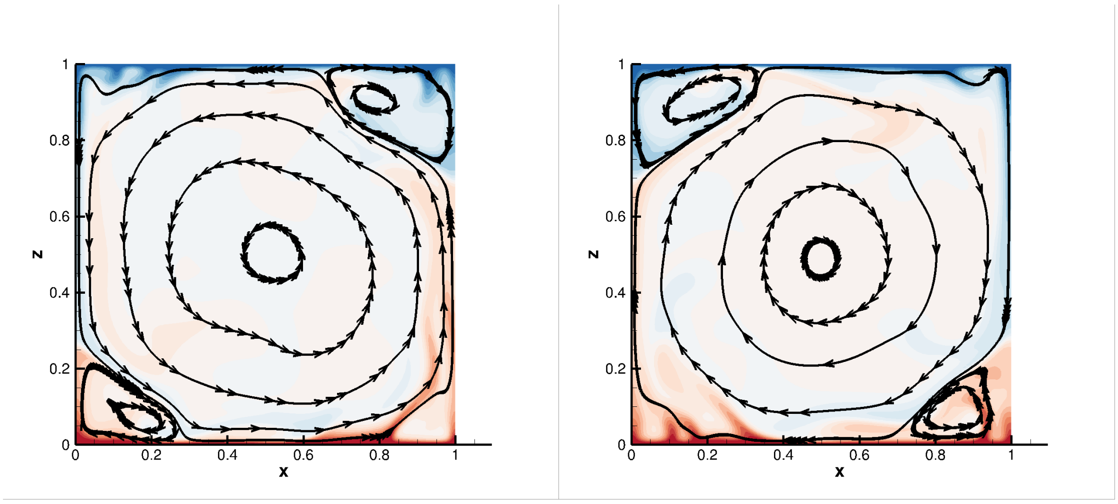

FIG. 1: Flow streamlines and temperature isocontours for two different realizations illustrating of the quasi-steady states of the flow at $Ra = 5\ 10^7$.

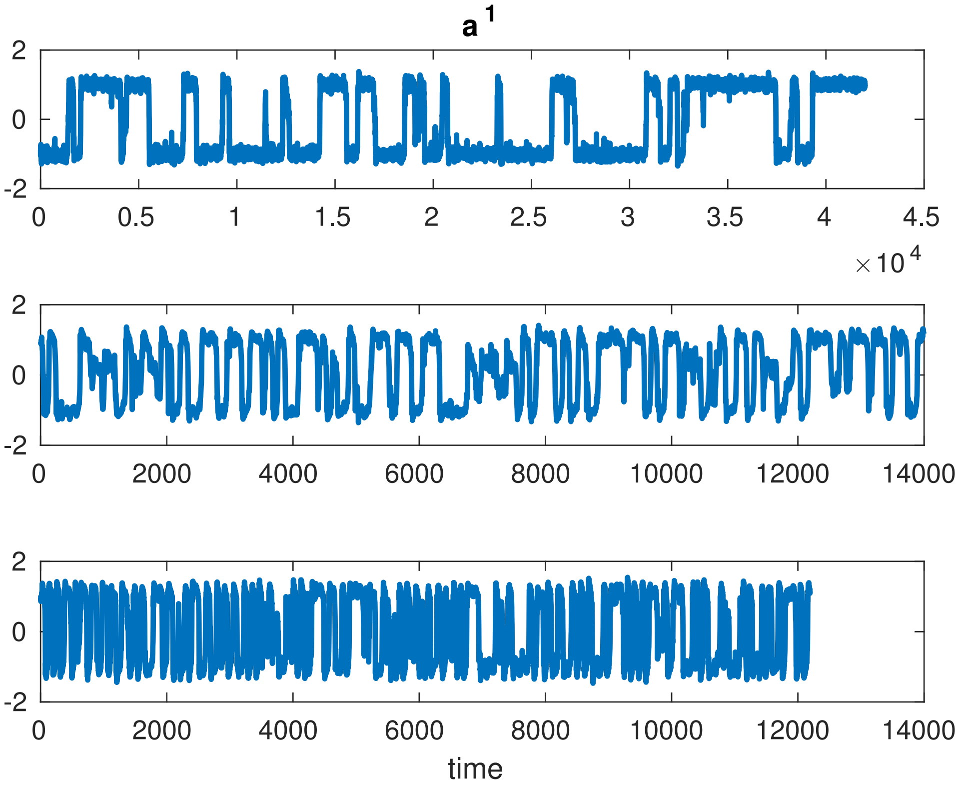

FIG. 2: Time evolution of first POD mode a^1. From top to bottom, $Ra = 3\ 10^7$, $Ra = 5\ 10^7$, $Ra = 10^8$.

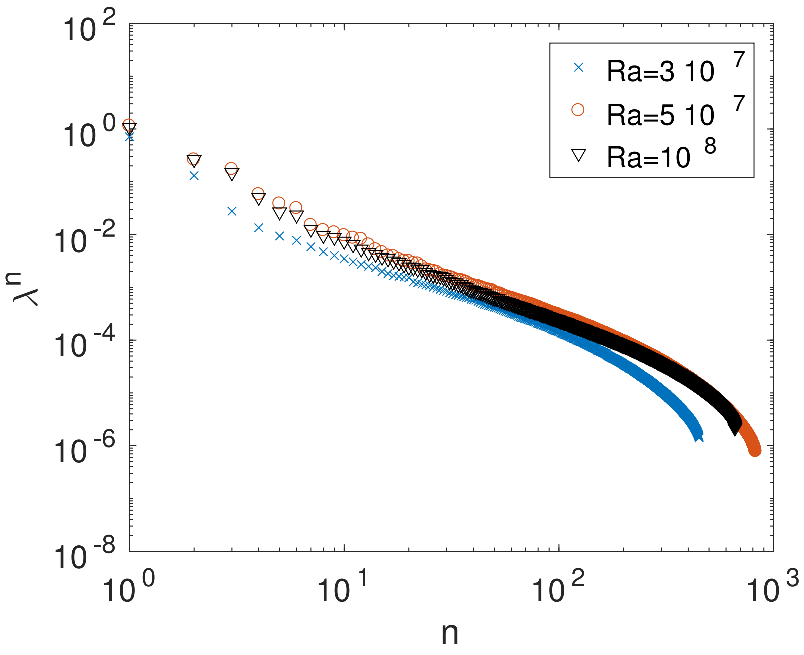

FIG. 3: POD spectrum at the different Rayleigh numbers

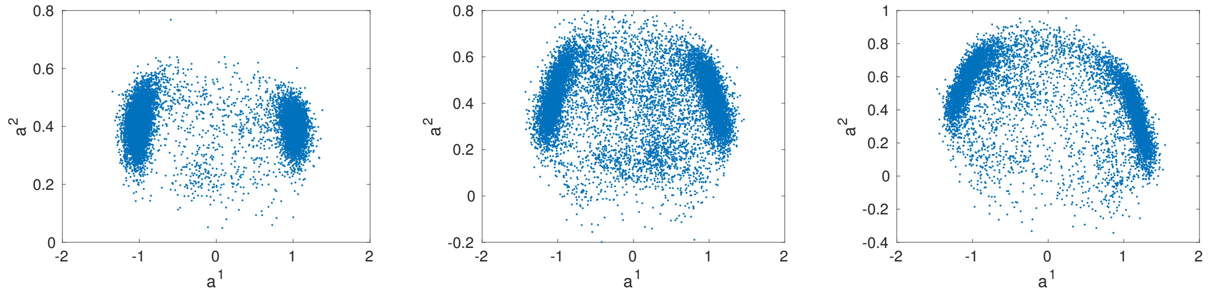

FIG. 4: Phase portraits for the first two POD modes a^1 and a^2. From left to right: $Ra = 3\ 10^7$, $Ra = 5\ 10^7$, $Ra = 10^8$.

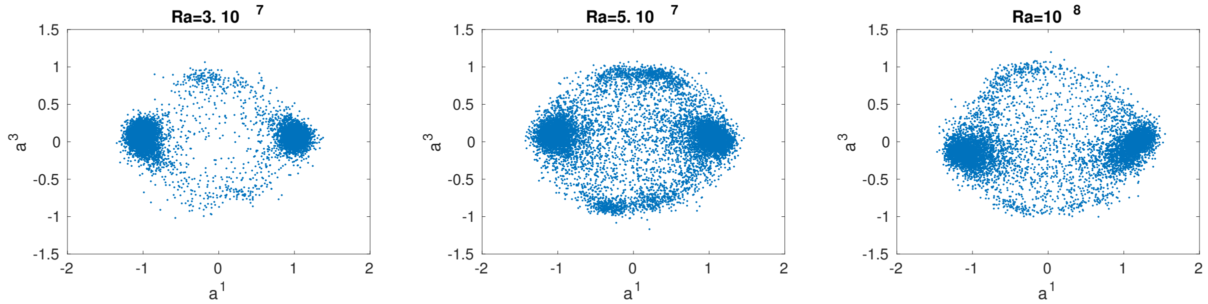

FIG. 5: Phase portraits for the two POD modes a^1 vs a^3; From left to right: $Ra = 3\ 10^7$, $Ra = 5\ 10^7$, $Ra = 10^8$.

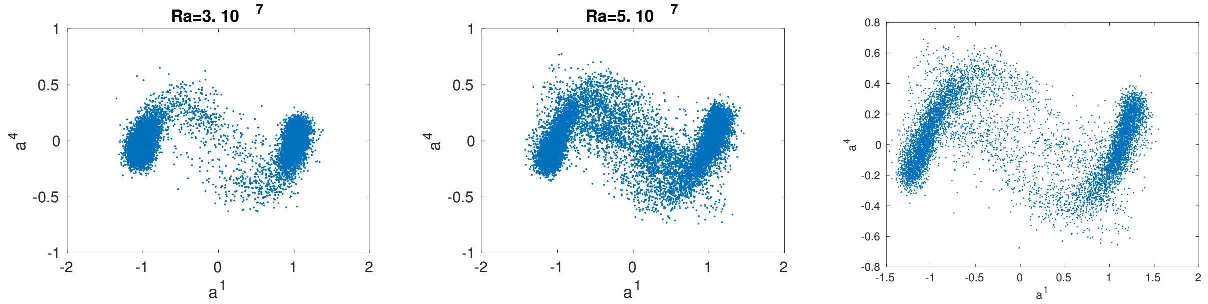

FIG. 6: Phase portraits for the two POD modes a^1 vs a^4; From left to right: $Ra = 3\ 10^7$, $Ra = 5\ 10^7$, $Ra = 10^8$.

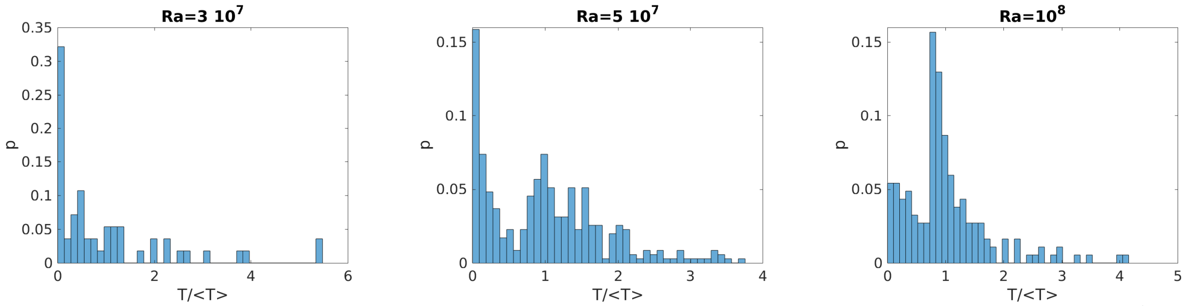

FIG. 7: Distribution of time (normalized by time-averaged value) between zeros of first POD mode a^1.

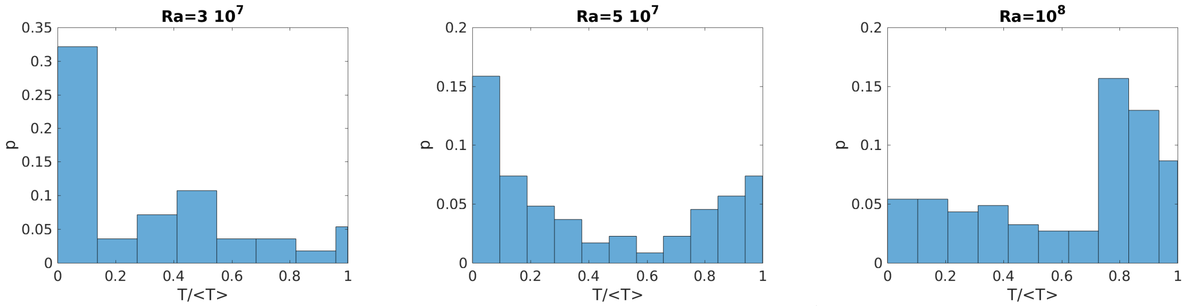

FIG. 8: Distribution of normalized time between zeros of first POD mode a^1 restricted to the time $[0, T/<T>]$.

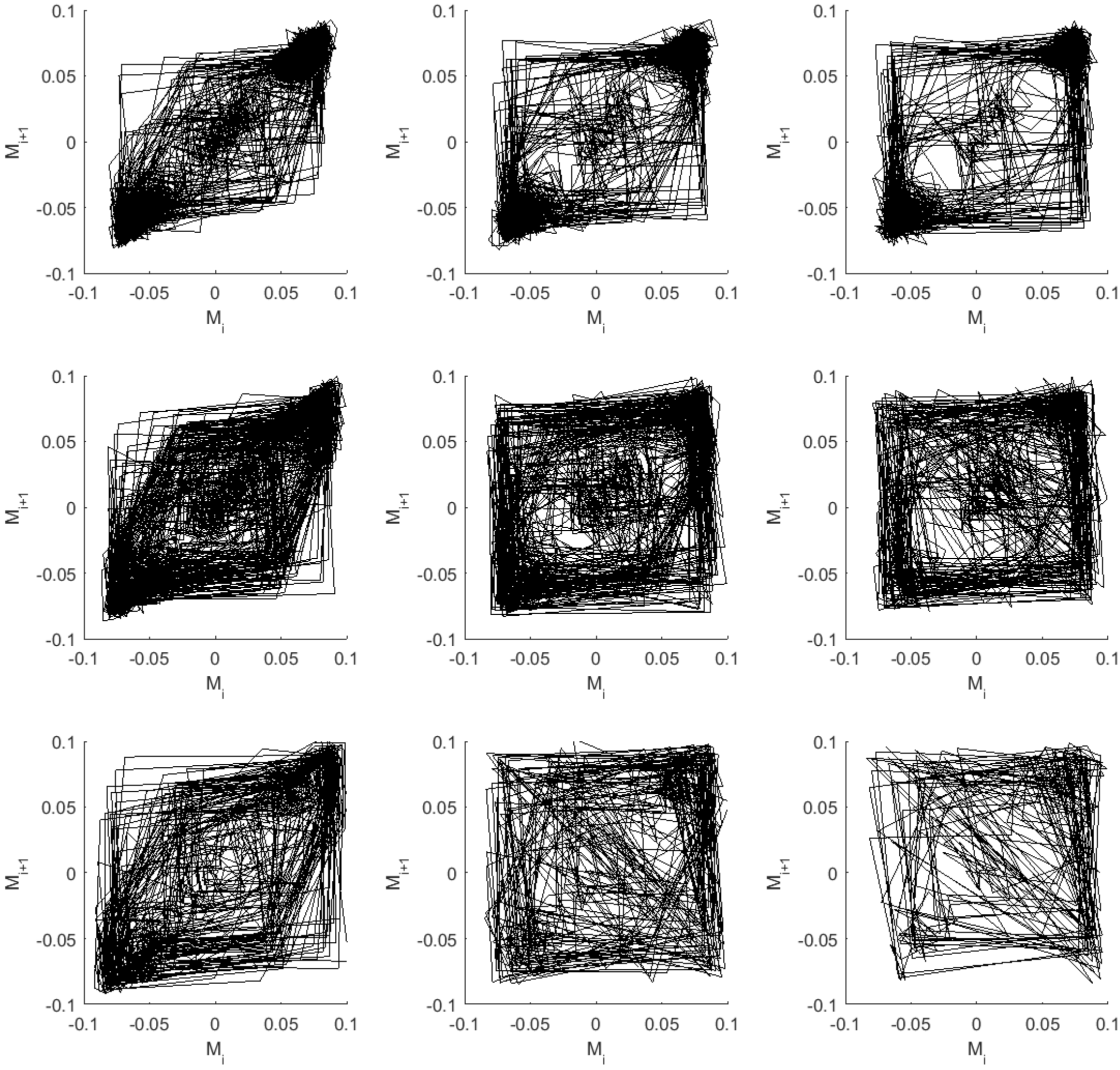

FIG. 9: Rayleigh Bénard attractors obtained at $Ra = 3 \cdot 10^7$ (top panels), $Ra = 5 \cdot 10^7$ (central panels), $Ra = 1 \cdot 10^8$ (bottom panels) varying Δt from $\Delta t = 3$ (left), $\Delta t = 6$ (center) and $\Delta t = 9$ (right).

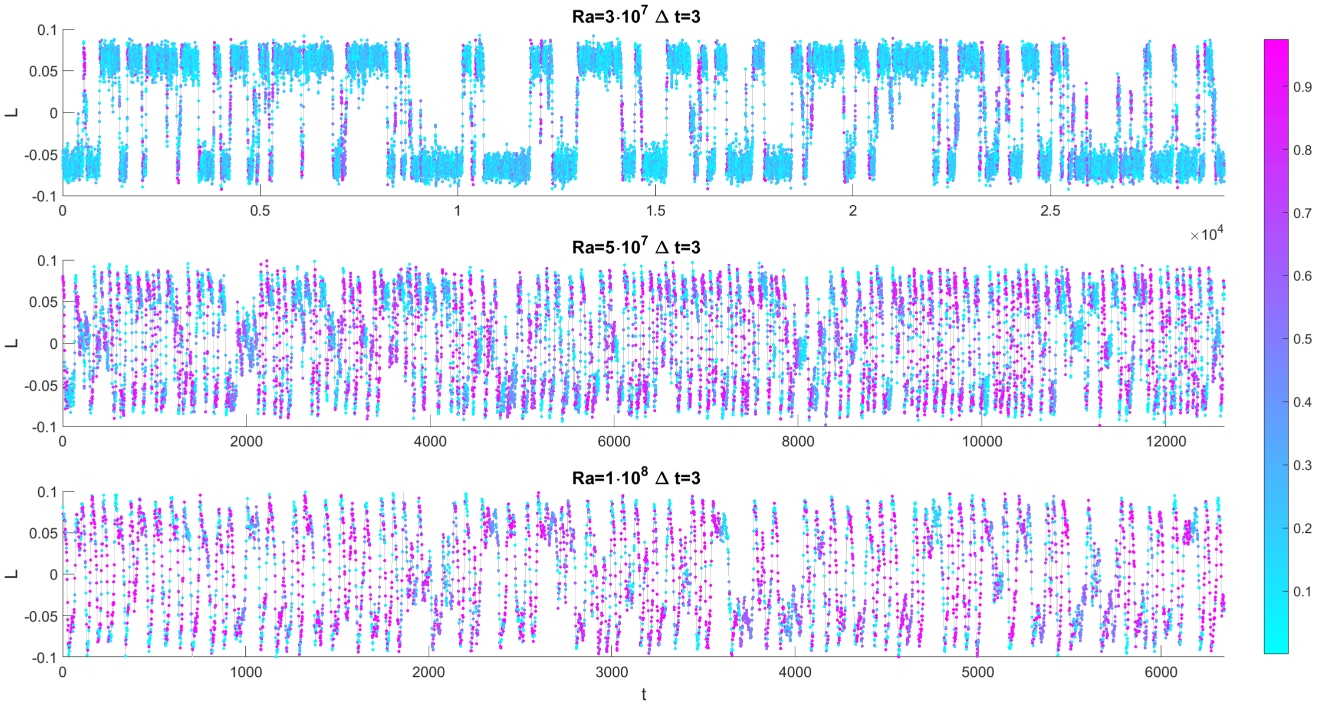

FIG. 10: Rayleigh Bénard time series obtained at $Ra = 3 \cdot 10^7$ (top panel), $Ra = 5 \cdot 10^7$ (central panel), $Ra = 1 \cdot 10^8$ (bottom panels) for $\Delta t = 3$. The colorscale represents the value of Υ.

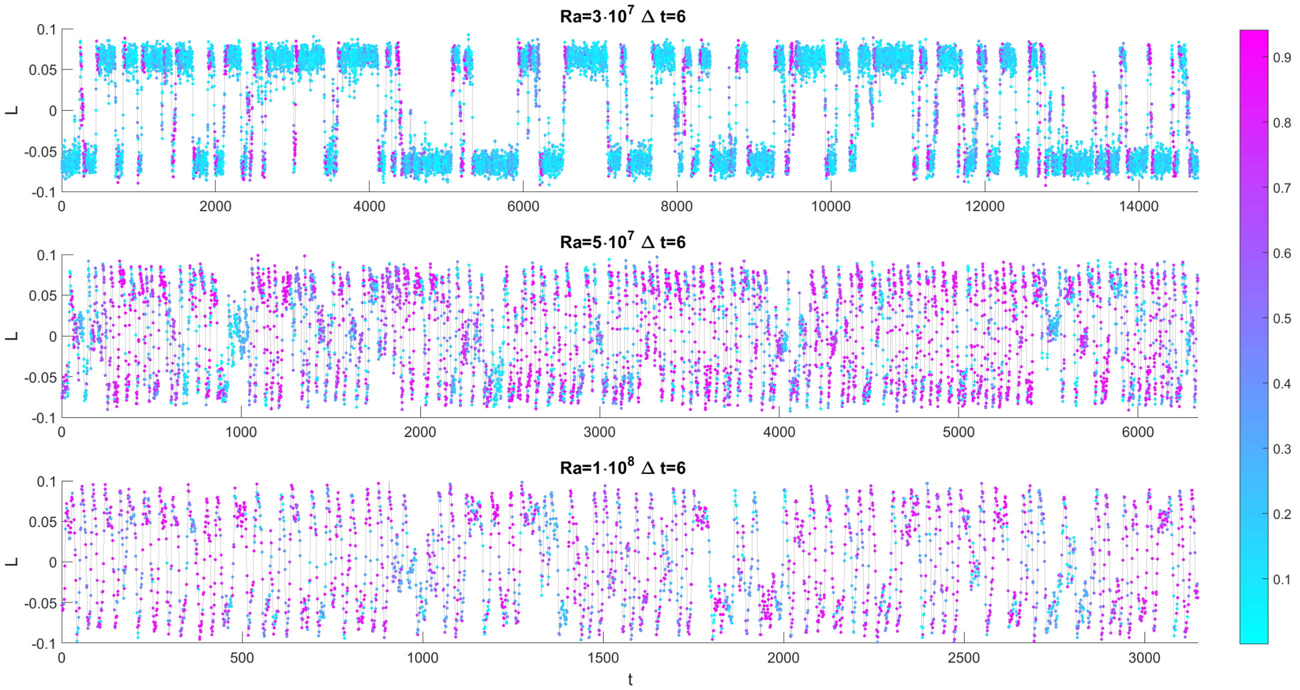

FIG. 11: Rayleigh Bénard time series obtained at $Ra = 3 \cdot 10^7$ (top panel), $Ra = 5 \cdot 10^7$ (central panel), $Ra = 1 \cdot 10^8$ (bottom panels) for $\Delta t = 6$. The colorscale represents the value of Υ

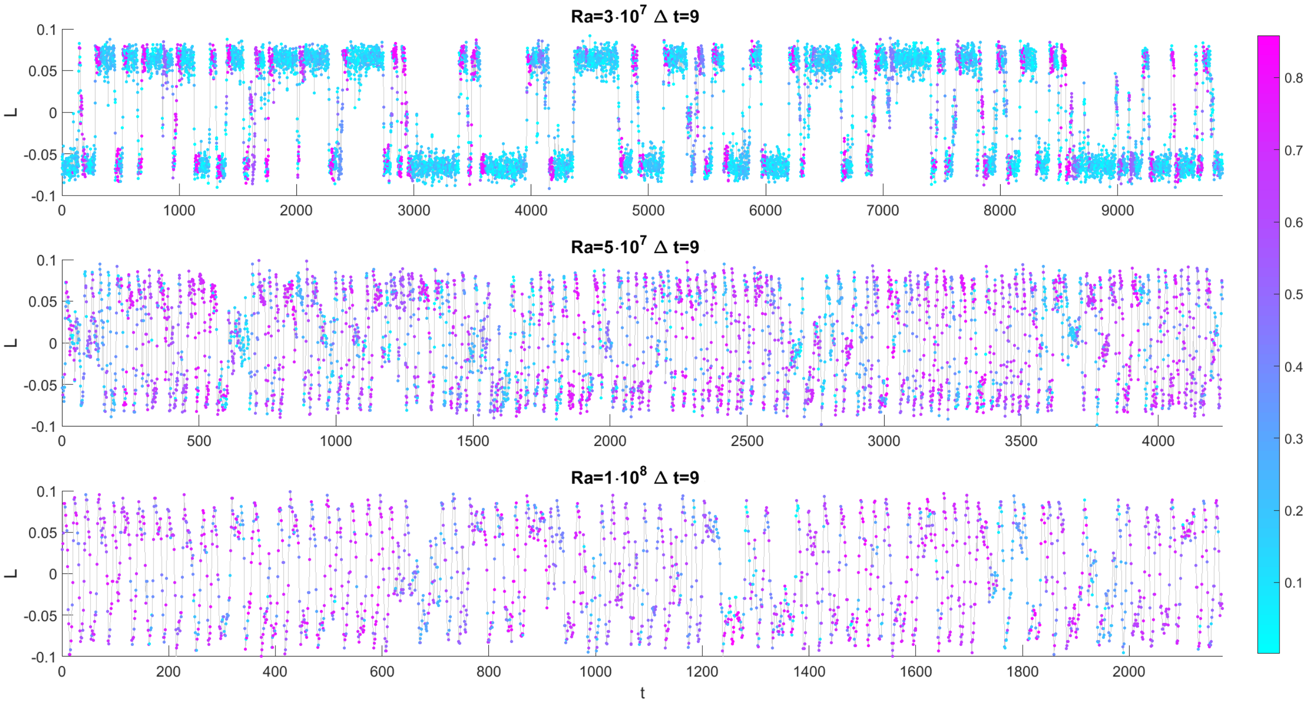

FIG. 12: Rayleigh Bénard time series obtained at $Ra = 3 \cdot 10^7$ (top panel), $Ra = 5 \cdot 10^7$ (central panel), $Ra = 1 \cdot 10^8$ (bottom panels) for $\Delta t = 9$. The colorscale represents the value of Υ

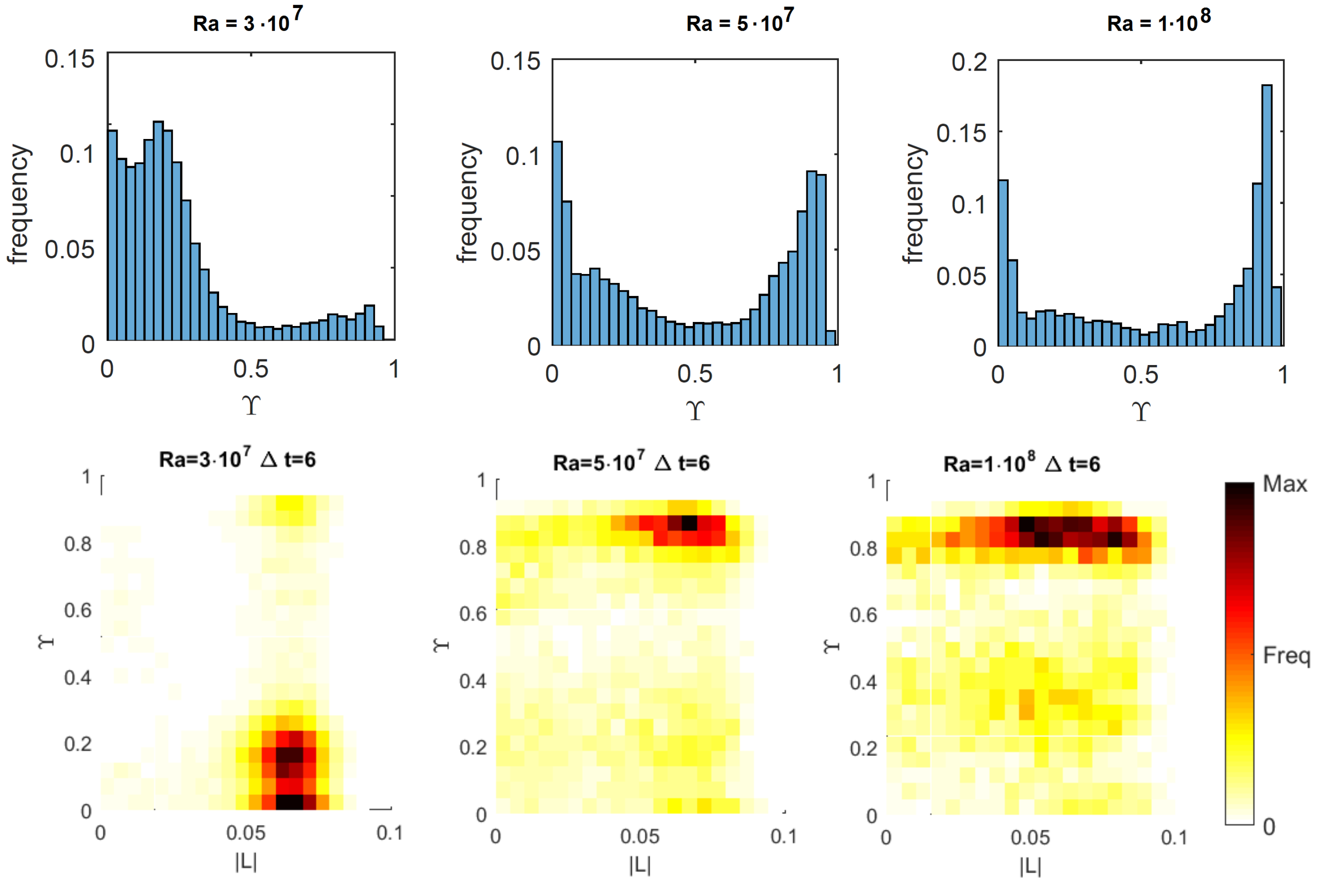

FIG. 13: Top panels: histograms of Υ for $Ra = 3 \cdot 10^7$ (left), $Ra = 5 \cdot 10^7$ (center), $Ra = 1 \cdot 10^8$ (right). Bottom panels: bivariate histograms Υ vs L.

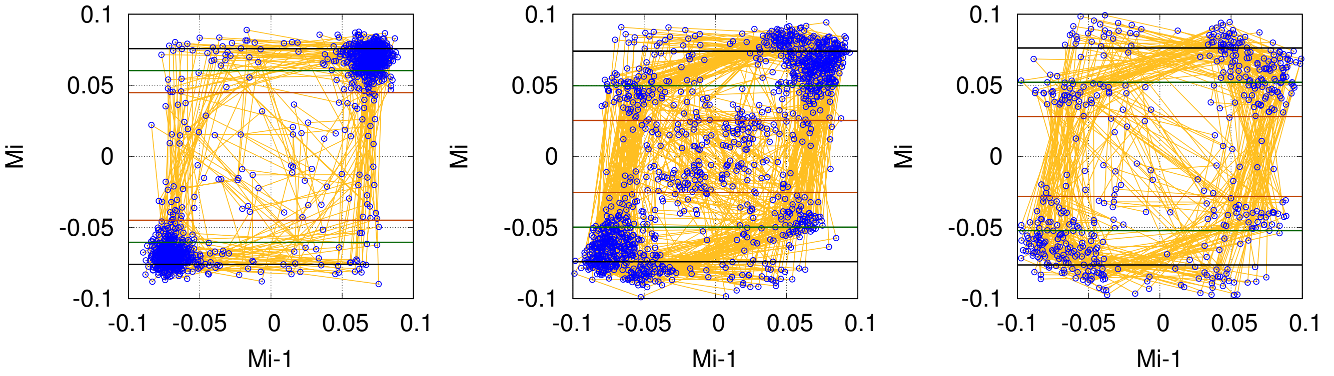

FIG. 14: Rayleigh Bénard attractors obtained at $Ra = 3 \cdot 10^7$ (left), $Ra = 5 \cdot 10^7$ (middle), $Ra = 10^8$ (right) with a time between subsequent peaks larger than twice the transition time τ_d ($\tau_d \sim 30, 12.5, 15$ convective time units for $Ra = 3 \cdot 10^7, 5 \cdot 10^7, 10^8$ respectively). Yellow lines show the paths between two subsequent (M_{i-1}, M_i) points.

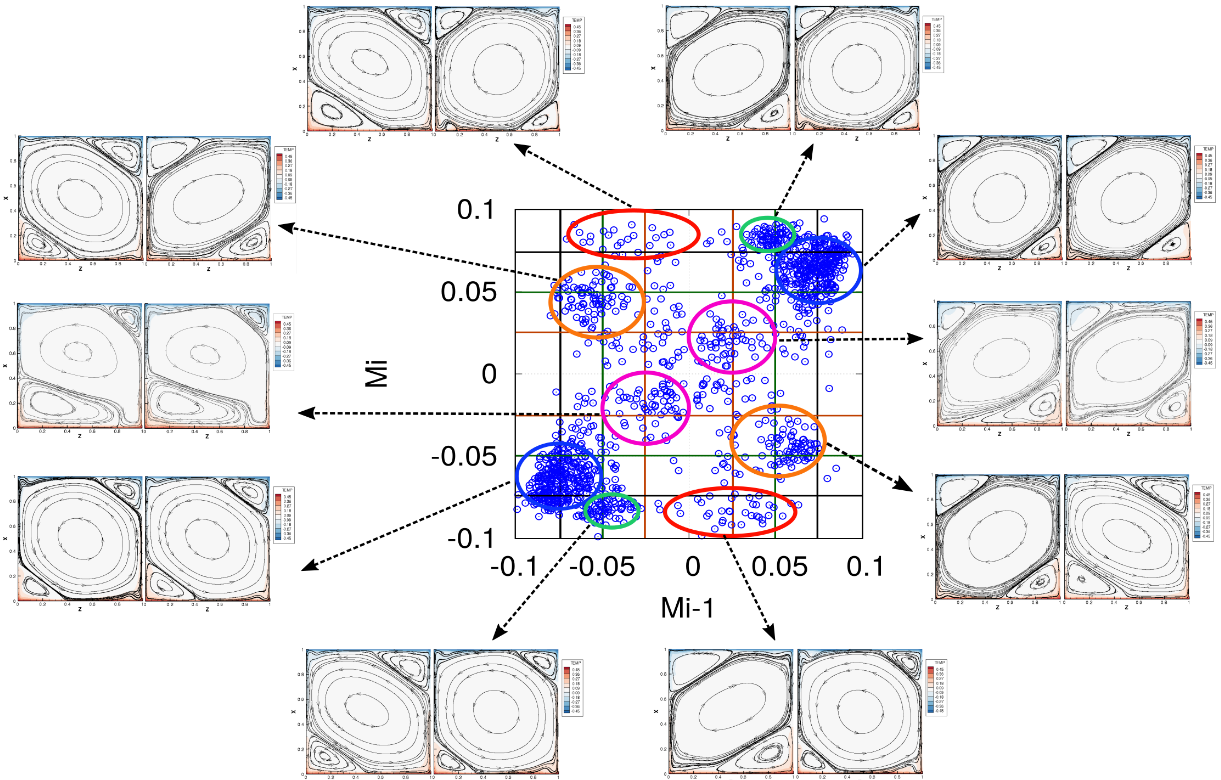

FIG. 15: Clusters in the Rayleigh Bénard attractor at $Ra = 5 \cdot 10^7$ and the related mean flow patterns at M_{i-1} (left) and M_i (right). Colour of cluster refers to the different regime or phases of the reversal cycle : first part of the release (orange), complete release (red), acceleration (green), accumulation (blue) and cessation (magenta). Flow pattern is shown by streamlines and temperature isocontours. Green, orange and black straight solid lines correspond to $|\bar{L}|$, $|\bar{L}| - \sigma(|L|)$ and $|\bar{L}| + \sigma(|L|)$ respectively.

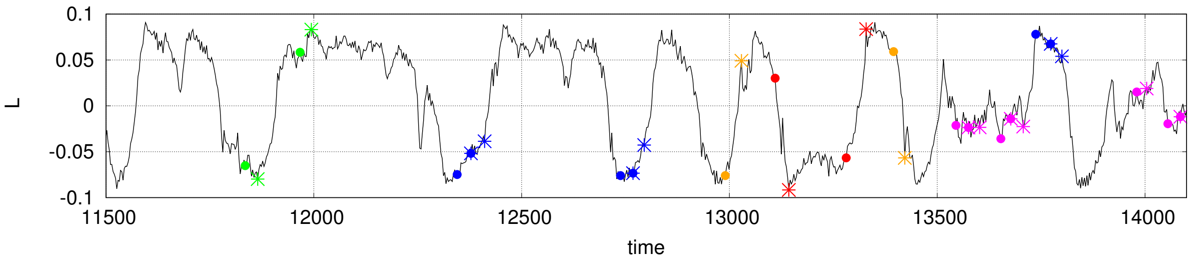

FIG. 16: Particular sequence of the angular momentum L time series at $Ra = 5 \cdot 10^7$. Colours refer to the different regime or phases of the reversal cycle : release (orange), after rebound (red), acceleration (green), accumulation (blue) and cessation (magenta). Markers give examples of the pairs (M_{i-1}, M_i) for each cluster: $\bullet$ (M_{i-1}), $*$ (Mi).

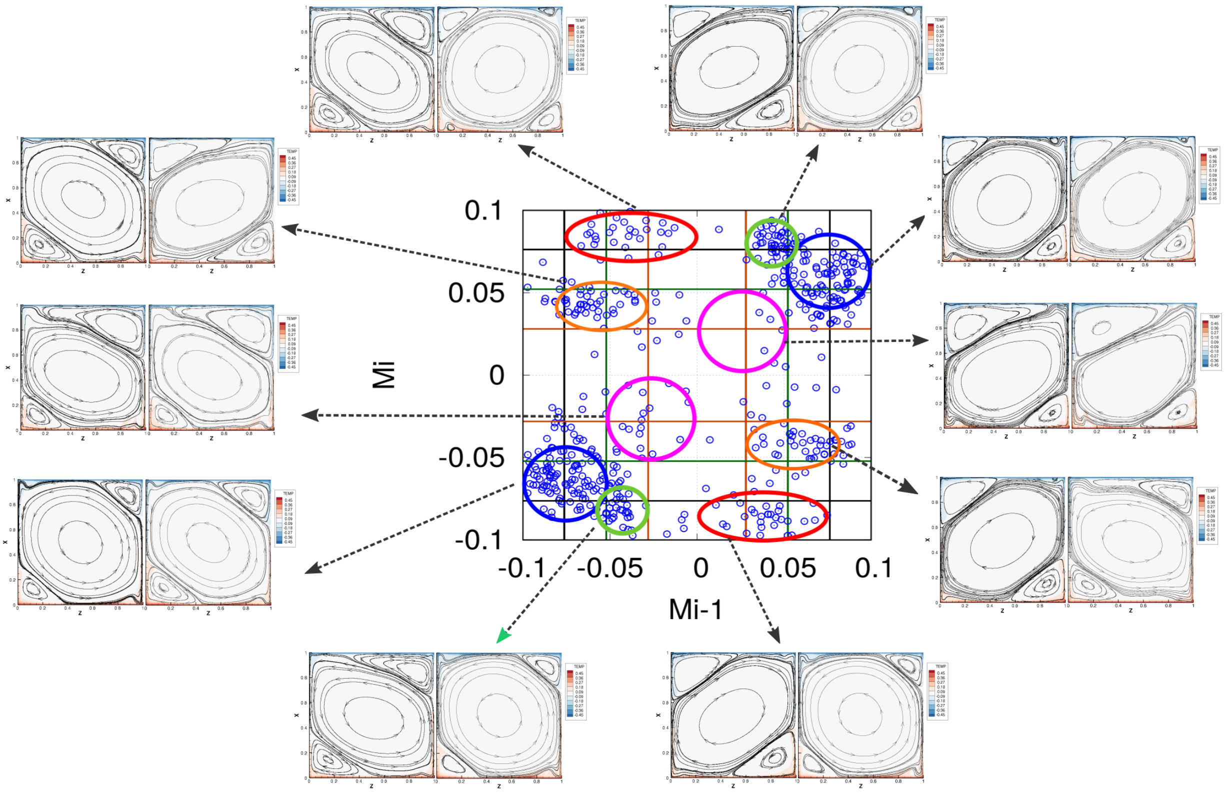

FIG. 17: Clusters in Rayleigh Bénard attractors at $Ra = 10^8$ and the related mean flow patterns. Same legend as in figure 15.

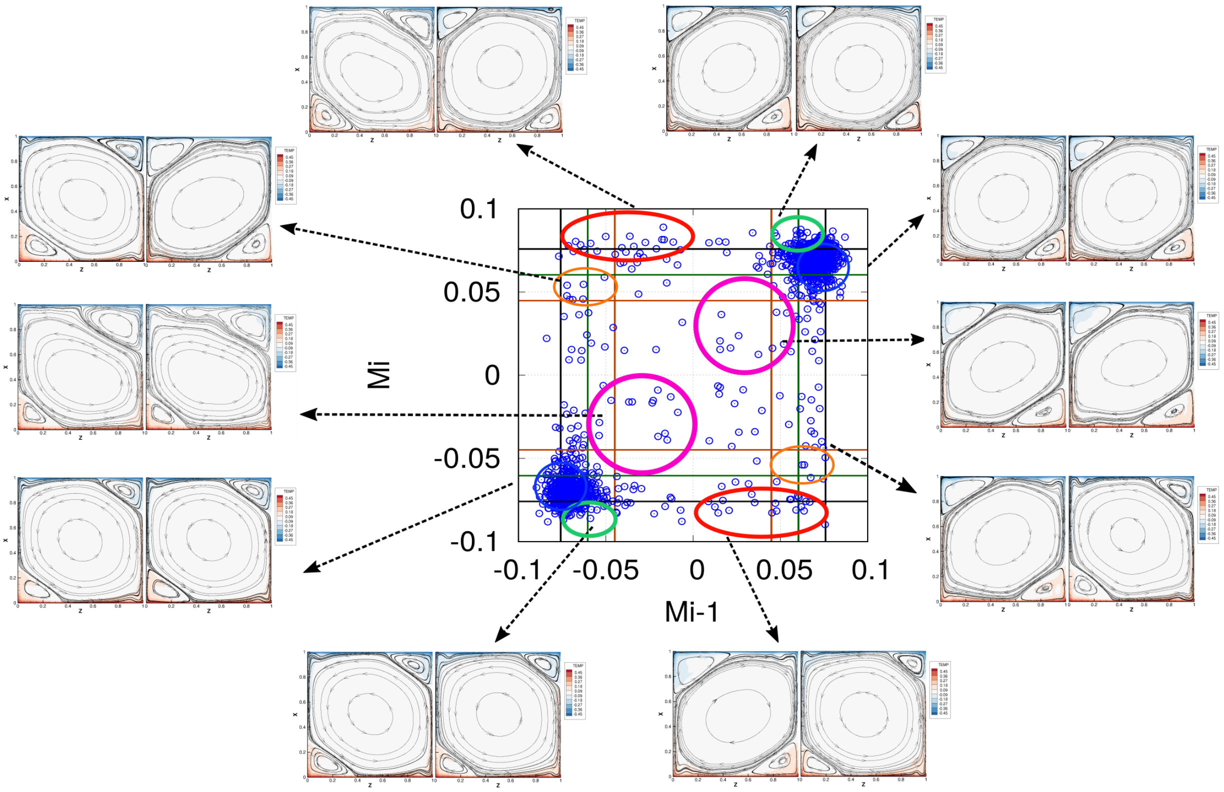

FIG. 18: Clusters in Rayleigh Bénard attractors at $Ra = 3 \cdot 10^7$ and the related mean flow patterns. Same legend as in figure 15.

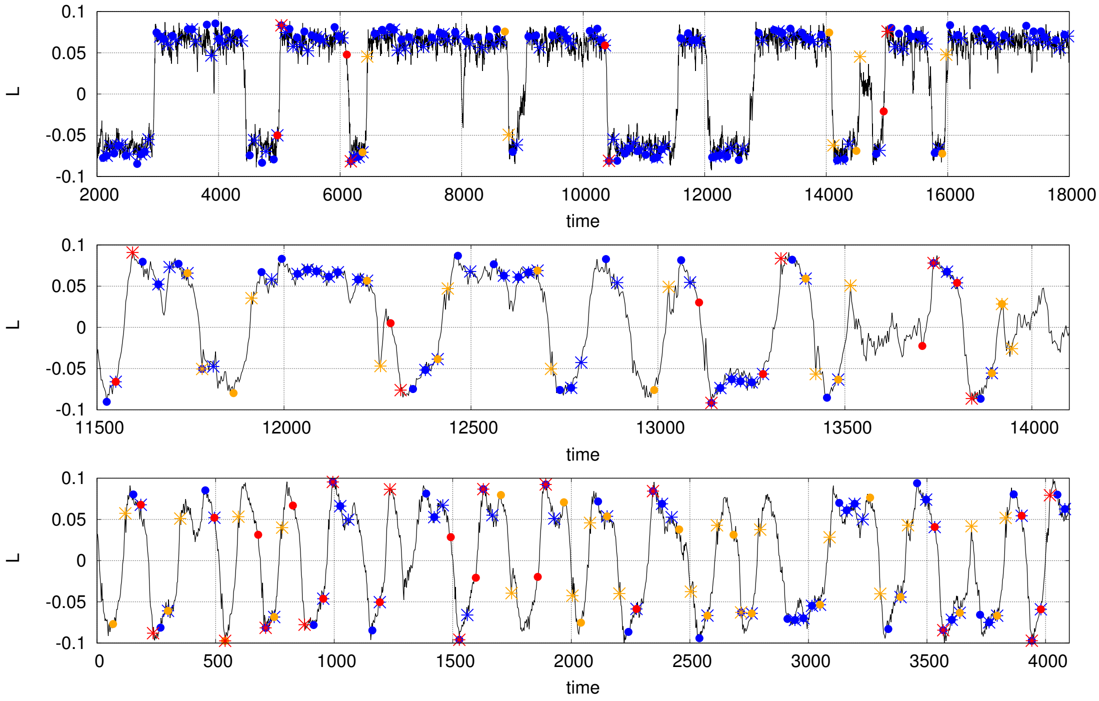

FIG. 19: Particular sequence of the angular momentum L time series at $Ra = 3 \cdot 10^7$, $Ra = 5 \cdot 10^7$ and $Ra = 10^8$. Markers give locations of all points contained inside the first part of release (orange), complete release (red) and accumulation (blue) clusters. $\bullet$ (M_{i-1}), $*$ (Mi) peaks.